Computationally efficient explicit nonlinear analyses using reduced integration-based solid-shell finite elements

M. Pagani [b,*], S. Reese [a], U. Perego [b]

[a] Institute of Applied Mechanics, RWTH Aachen University, D-52074 Aachen, Germany
[b] Department of Structural Engineering, Politecnico di Milano, I-20133 Milano, Italy

Article history:
Received 7 December 2012
Received in revised form 10 June 2013
Accepted 3 September 2013
Available online 19 September 2013

1. Introduction

Solid-shell formulations based on reduced integration with hourglass stabilization exhibit many advantages which make them attractive for the use in challenging applications, e.g. in production technology, electronics and crash simulation. Among these positive aspects is the possibility to take the thickness deformation into account in a straightforward way, which facilitates the implementation of general three-dimensional material models. This is especially important for contact modelling. Solid-shells possess only displacement degrees-of-freedom which significantly facilitates the coupling with other finite element formulations, in particular solids. See for more information the papers of e.g. (alphabetical order) [1,7,12,32,34]. Besides the last mentioned paper, these works include only implicit analyses.

* Corresponding author.
E-mail address: pagani@stru.polimi.it (M. Pagani).

An important aspect of solid-shells based on reduced integration is obviously the fact that less Gauss points are needed. This property becomes especially valuable in the context of explicit simulations where the computational effort is directly proportional to the number of Gauss points. However, on the other hand, just in explicit simulations the critical time is determined by the smallest dimension of an element. In contrast to a finite element discretization based on four-node shells, for solid-shells the thickness becomes relevant. In many situations the latter is smaller than the smallest dimension of an element in the shell middle plane. One goal of the present paper is to exploit the advantage of a minimum number of Gauss points while simultaneously coping with the problem that the critical time step is controlled by the thickness of the structure.

Several recently published contributions show that there is a growing interest in the use of solid-shell elements in explicit dynamics simulations (see e.g. [34,23,20,21,37,24]). However, the solid-shell technology is a rather new development and there is only little experience concerning its performance in an explicit context. In Mattern and Schweizerhof [23] and Mattern et al. [24], it is shown that using solid-shells in combination with the enhanced assumed strain (EAS) method leads to high computational effort at the element level because the additional degrees-of-freedom are usually determined by means of static condensation. To overcome the problem the authors treat these degrees-of-freedom "as regular unknowns in the global equations". This requires to introduce an artificial lumped mass matrix. In order to avoid possible non-physical effects due to this matrix the kinetic energy associated with the additional unknowns is controlled. Also [34] show that a good agreement between the results of implicit and explicit analysis can be obtained. They concentrate on multilayered structures. Both geometrical as well as material non-linearities are included. Related to the present paper are further the contributions of Pagani et al [30] and Cocchetti et al. [9] where a new method of selective mass scaling is proposed together with an analytical estimate of the scaled element maximum eigenfrequency, applicable to undistorted or slightly distorted elements. It is based on the idea to modify the higher order modes which restrict the critical time step but are usually not relevant for the solution. This concept is customarily used also for classical four-node shell elements, where masses pertinent to rotational degrees of freedom are usually increased (see e.g. [15]). Note that a similar mass scaling procedure, applied to solid elements, has been pursued earlier by Olovsson and coauthors (see [28], and also [29]) without however providing an effective procedure for the computation of the scaled element maximum eigenfrequency. In general it can be said that selective mass scaling is used to reduce the speed of sound in thickness direction without affecting the in-plane traversal time. This leads to a smaller maximum eigenfrequency at the element level and consequently to a larger critical time step. For completeness, we additionally like to mention the classical and important work on explicit integration by Belytschko et al. [2]. The authors use four-node shells (i.e. no solid-shells) in combination with reduced quadrature. Flanagan and Belytschko [11] furnish estimates for the computation of the maximum element eigenfrequency. Other updated references to existing mass scaling techniques can be found in Cocchetti et al. [9].

Explicit simulation becomes important in many different fields of application. Bergmann and Oldenburg [3] suggest a staggered approach for coupling explicit thermal and mechanical analyses of sheet metal forming. Important is here that the minimum time step of the mechanical part of the analysis is much smaller than the one for the thermal part. Also these authors mention mass scaling as a method to overcome the problem. The paper, however, does not include a new approach to this method. In the paper of Hetherington and Askes [14] the effect of stiffness as well as inertial penalties on the critical time step is investigated. Whereas stiffness penalties reduce the critical time step which is a major disadvantage, inertial penalties have a positive effect which may allow for an increase in the time step. The disadvantage is however that the penalized mass matrix is no longer diagonal, which represents a significant drawback in explicit approaches. Harwood and McHugh [13] compare implicit and explicit finite element methods in the context of crystal plasticity. Their results show that the explicit method is computationally preferable if parallelization is possible. Further, the explicit simulation is more robust if contact is involved. Classical uniform mass scaling is used to reduce the runtime. To avoid non-physical results, the amount of kinetic energy is controlled. Standard uniform mass scaling is also conducted by Wang et al. [36]. Vrh et al. [35] suggest an improved explicit integration scheme for a constitutive model of elasto-plasticity. Its main advantage is that the consistency condition can be fulfilled along the entire integration path. The solder joint reliability in electronics under shock and vibration is investigated by Lall et al. [19]. These authors testify the higher robustness of explicit methods in the context of wave propagation problems. They further investigate the performance of different element formulations and conclude that for their examples lower order elements are better suitable than higher order ones. Another result of their work is that reduced integration is a good means to decrease the computational effort. A similar argumentation is found in the paper of Ma and Liu [22]. More application oriented is the work of Bisagni [5] where explicit methods are applied to investigate the dynamic buckling of fiber reinforced plastics shell structures.

In summary, there are several groups of authors who apply explicit methods in different contexts. However, the issue of finite element technology comes into play only in very few of these publications. Especially the use of solid-shell formulations in explicit analysis deserves attention.

In the present paper, the explicit dynamics implementation of an 8-node solid-shell element, denominated Q1STS, recently proposed by Schwarze and Reese in an implicit context [32] is critically analyzed. Both linear and nonlinear problems are considered, including finite deformations, elastoplasticity and contact. The element is based on a reduced integration with hourglass control and implements ANS (Assumed Natural Strain) and EAS technologies to avoid the various types of locking behavior that affect this type of low order solid-shell elements. In particular, three aspects which can become computationally critical in explicit dynamics are addressed: frequency of the hourglass control update, computation of the enhanced strain parameter and critical time step size. The computational efficiency of various options, including the

already mentioned recently proposed selective mass scaling technique, which in Cocchetti et al. [9] was applied to a different type of solid-shell element, is comparatively investigated through a series of numerical tests. A new strategy for the optimal choice of the mass scaling parameter is also proposed and numerically verified.

The paper is structured as follows. In Section 1, we summarize the key points of the solid-shell formulation used in the paper. Section 2 includes a summary of the method of selective mass scaling and the presentation of the new strategy for the selection of the mass scaling parameter. Finally, we come in Section 3 to a large variety of numerical examples, reaching from simple structures such as a beam to metal forming. Linear-elastic as well as elasto-plastic material behavior is considered.

2. Solid-shell formulation based on EAS and ANS concepts

The present paper aims to show how innovative solid-shell finite element technology can be applied in the explicit solution of problems of structural mechanics. We concentrate here on a recent formulation of an 8-node hexahedron denominated Q1STS, proposed by Schwarze and Reese [32] which exploits the concept of reduced integration with hourglass stabilization in a special way. To avoid volumetric and Poisson thickness locking the enhanced assumed strain (EAS) method is included. Further, in order to improve the performance of the element for very thin structures, in particular to eliminate transverse shear and curvature thickness locking, we additionally integrate the assumed natural strain (ANS) concept. The most important ingredients of this finite element technology are discussed in what follows. Thereby, we put special emphasis on its application in explicit simulation.

2.1. Continuous weak form

The present finite element formulation departs from the two-field functional used in many enhanced strain approaches. See the pioneering work of Simo and Armero [33] but also many more applications of this variational functional (see e.g. [17,25,31,8]). The mentioned papers can be split into so-called "**F**-based" (**F** deformation gradient) and "**E**-based" (**E** Green–Lagrange strain tensor) concepts. According to our knowledge the literature offers only a few papers (see e.g. [10]) where the ANS method is implemented into an **F**-based approach. Most other publications exploit the additive split of $\mathbf{E} = \mathbf{E}_c + \mathbf{E}_e$ into compatible ($\mathbf{E}_c$) and enhanced ($\mathbf{E}_e$) parts [34,16,18]. Accordingly the two equations of weak form read

$$g_1(\mathbf{u}, \mathbf{E}_c) = \int_{B_0} \mathbf{S}(\mathbf{E}) \cdot \delta\mathbf{E}_c \, dV + \int_{B_0} \rho_0 \ddot{\mathbf{u}} \cdot \delta\mathbf{u} \, dV + g_{\text{ext}} = 0 \tag{1}$$

$$g_2(\mathbf{u}, \mathbf{E}_e) = \int_{B_0} \mathbf{S}(\mathbf{E}) \cdot \delta\mathbf{E}_e \, dV = 0 \tag{2}$$

where B_0 refers to the domain of the undeformed configuration (ρ_0 and dV being the corresponding mass density and infinitesimal volume element, respectively), $\mathbf{u}$ denotes the displacement vector and $\mathbf{S}$ the second Piola–Kirchhoff stress tensor. The term g_{ext} refers to the virtual work of the external loading. Most inelastic material models are structured in such a way that their internal variables represent implicit functions of $\mathbf{E}$. Thus, writing $\mathbf{S}$ as sole function of $\mathbf{E}$ lets us include here also the case of inelastic material behavior.

2.2. Split into physically relevant and hourglass parts

Split of stress. To simplify the integrals appearing in (1) and (2), we split the second Piola–Kirchhoff stress tensor

$$\mathbf{S} = \mathbf{S}^{\star} + \mathbf{S}^{\text{hg}} \tag{3}$$

into two terms, where the first one ($\mathbf{S}^{\star}$) is a non-linear function of the local thickness coordinate ζ and the second one ($\mathbf{S}^{\text{hg}}$) a linear function of all three local element coordinates ξ, η and ζ. Note that from now on we will use Voigt notation indicated by a hat over a quantity. For the two stress parts we write $\hat{\mathbf{S}}^{\star}$ and $\hat{\mathbf{S}}^{\text{hg}}$, respectively. It should already be explained at this point that the stress $\hat{\mathbf{S}}^{\star}$ will include the constitutive modelling evaluated in the Gauss points of the element. As such, it crucially influences the quantitative result of a problem. It represents the so-called "physically relevant" part of the stress tensor $\hat{\mathbf{S}}$. In contrast, the "hourglass" stress $\hat{\mathbf{S}}^{\text{hg}}$ is only needed to "stabilize" the element and should be computed as efficiently as possible. Its influence on the results vanishes with increasing mesh density. But the "choice" of $\hat{\mathbf{S}}^{\text{hg}}$ has to be well balanced. Too large values lead to locking, too small values to hourglass instabilities. For this reason it is important to develop a physically-based method to compute this part of the stress. Manual choices which are partly still possible in commercial finite element program systems easily cause erroneous results, in particular for inelastic material behavior. Additional questions arise in explicit simulations where the time step size has to be extremely small and the cost of repeated computations at element level may soon become excessive. As it will be shown below, the hourglass stress depends on the current element state and in principle it has to be updated regularly to prevent the development of hourglass modes. However, the system changes in a time step are very small and it is expected that the update of the hourglass stiffness does not have to be done in every time step. A suitable strategy for updating it in non-consecutive time steps must take the special characteristics of the underlying finite element technology into account. This will be investigated in Sections 4.1 and 4.2.

The additive decomposition of $\hat{\mathbf{S}}$ is achieved by a Taylor expansion of $\hat{\mathbf{S}}$ with respect to the position $\boldsymbol{\xi}^\star = \{0,0,\zeta\}^T$ (the vector $\boldsymbol{\xi}$ being given by $\boldsymbol{\xi} = \{\xi,\eta,\zeta\}^T$). The vector $\boldsymbol{\xi}^\star$ crosses the centre of the element and is directed in the thickness direction ζ. The higher order terms in the Taylor expansion are neglected. We can write

$$\hat{\mathbf{S}} \approx \underbrace{\hat{\mathbf{S}}\Big|_{\boldsymbol{\xi}^\star}}_{\hat{\mathbf{S}}^\star} + \frac{\partial \hat{\mathbf{S}}}{\partial \hat{\mathbf{E}}}\frac{\partial \hat{\mathbf{E}}}{\partial \xi}\bigg|_{\boldsymbol{\xi}^\star} \xi + \frac{\partial \hat{\mathbf{S}}}{\partial \hat{\mathbf{E}}}\frac{\partial \hat{\mathbf{E}}}{\partial \eta}\bigg|_{\boldsymbol{\xi}^\star} \eta \tag{4}$$

The first term is the desired $\hat{\mathbf{S}}^\star$. The second part, however, depends via $\hat{\mathbf{C}} = \partial \hat{\mathbf{S}}/\partial \hat{\mathbf{E}}$ still non-linearly on ζ. To circumvent this problem we replace the matrix $\hat{\mathbf{C}}$ by a constant matrix $\hat{\mathbf{C}}^{\mathrm{hg}} = \mu_{\mathrm{eff}}^{\mathrm{hg}}\, \hat{\mathbf{I}}^{\mathrm{dev}}$. In the latter relation $\hat{\mathbf{I}}^{\mathrm{dev}}$ represents the Voigt notation of the fourth order tensor $\mathcal{I}^{\mathrm{dev}} = \mathcal{I} - (1/3)\mathbf{I}\otimes\mathbf{I}$ where $\mathcal{I}$ and $\mathbf{I}$ are the fourth and second order identity tensors, respectively. The deviatoric character of the matrix $\hat{\mathbf{C}}^{\mathrm{hg}}$ is needed to eliminate volumetric locking. For the computation of the parameter $\mu_{\mathrm{eff}}^{\mathrm{hg}}$ see Remark 1. Since we have not yet derived the interpolation of $\hat{\mathbf{E}}$ we are not yet in the position to determine $\hat{\mathbf{S}}^{\mathrm{hg}}$. Consequently, the interpolation of $\hat{\mathbf{E}}$ is the next step.

Split of compatible strain. In general we seek to describe the hourglass stress and both strain parts $(\mathbf{E}_c, \mathbf{E}_e)$ by means of polynomials. This will enable us to reduce the volume integrals in (1) and (2) to line integrals. Let us consider first the compatible strain $\hat{\mathbf{E}}_c$ which we require to be represented by

$$\hat{\mathbf{E}}_c = \underbrace{\hat{\mathbf{E}}_c^0 + \zeta\hat{\mathbf{E}}_c^\zeta + \zeta^2\hat{\mathbf{E}}_c^{\zeta\zeta}}_{\hat{\mathbf{E}}_c^\star} + \underbrace{\xi\hat{\mathbf{E}}_c^\xi + \eta\hat{\mathbf{E}}_c^\eta + \xi\eta\hat{\mathbf{E}}_c^{\xi\eta} + \eta\zeta\hat{\mathbf{E}}_c^{\eta\zeta} + \zeta\xi\hat{\mathbf{E}}^{\zeta\xi}}_{\hat{\mathbf{E}}_c^{\mathrm{hg}}} \tag{5}$$

where the vectors $\hat{\mathbf{E}}_c^\bullet$ and $\hat{\mathbf{E}}_c^{\bullet\bullet}$ $(\bullet = \xi,\eta,\zeta)$ are element-wise constant. Analogously to the split of $\hat{\mathbf{S}}$, we see in the first term a non-linear dependence on ζ, in the second term a linear dependence on ξ,η and ζ. The question is now how $\hat{\mathbf{E}}_c^\bullet$ and $\hat{\mathbf{E}}_c^{\bullet\bullet}$ are determined.

For this purpose we introduce the two sets of base vectors $\mathbf{e}_i$ and $\mathbf{H}_i = \partial\xi_i/\partial\mathbf{X}$ $(i = 1,2,3)$. In the latter relation, we represent the local coordinates by means of $\xi_1 = \xi, \xi_2 = \eta$ and $\xi_3 = \zeta$. The vector $\mathbf{X}$ refers to the position of a point in the undeformed configuration. It is now possible to formulate the tensor $\mathbf{E}_c$ either with respect to the cartesian basis $\mathbf{e}_i$ or using the basis $\mathbf{H}_i$ $(i = 1,2,3)$:

$$\mathbf{E}_c = (E_c)_{ij}\,\mathbf{e}_i\otimes\mathbf{e}_j = (\bar{E}_c)_{ij}\,\mathbf{H}_i\otimes\mathbf{H}_j \tag{6}$$

Note that we assume Einstein's summation convention to hold. In the case of an element with the sidelengths $2\ \times 2\times 2$ the coefficients $(E_c)_{ij}$ and $(\bar{E}_c)_{ij}$ are identical. Working with the classical trilinear isoparametric shape functions it is evident that $(\bar{E}_c)_{ij}$ are polynomials. At this point the ANS concept comes into play. Proceeding as suggested by Betsch and Stein [4,6] we replace the thickness strain $(\bar{E}_c)_{33}$ by its ANS interpolation which eliminates curvature thickness locking. The ANS method is additionally applied to the transverse shear terms $(\bar{E}_c)_{23}$ and $(\bar{E}_c)_{31}$ to work against transverse shear locking. More details are given in Bischoff and Ramm [32]. Using Voigt notation we can further write $\hat{\mathbf{E}}_c = \mathbf{T}\hat{\bar{\mathbf{E}}}_c$ where the transformation matrix $\mathbf{T}$ is in general a complex rational function of the local coordinates. Thus, without further simplification, $\hat{\mathbf{E}}_c$ would also contain rational functions of ξ,η and ζ. This is the situation which we seek to avoid. We achieve that by working with a polynomial approximation of $\mathbf{T}$ which reads $\mathbf{T} \approx \mathbf{T}^0 + \xi\mathbf{T}^\xi + \eta\mathbf{T}^\eta + \zeta\mathbf{T}^\zeta$. Thus, all terms of $\mathbf{T}$ which depend on quadratic and higher order combinations of the local coordinates are omitted.

Representing $\hat{\bar{\mathbf{E}}}_c$ in a form analogous to (5) lets us finally write

$$\begin{aligned}
&\hat{\bar{\mathbf{E}}}_c^0 = \mathbf{T}^0\hat{\bar{\mathbf{E}}}_c^0, \quad \hat{\bar{\mathbf{E}}}_c^\zeta = \mathbf{T}^0\hat{\bar{\mathbf{E}}}_c^\zeta + \mathbf{T}^\zeta\hat{\bar{\mathbf{E}}}_c^0, \quad \hat{\bar{\mathbf{E}}}_c^{\zeta\zeta} = \mathbf{T}^0\hat{\bar{\mathbf{E}}}_c^{\zeta\zeta} + \mathbf{T}^\zeta\hat{\bar{\mathbf{E}}}_c^\zeta,\\
&\hat{\bar{\mathbf{E}}}_c^\xi = \mathbf{T}^0\hat{\bar{\mathbf{E}}}_c^\xi + \mathbf{T}^\xi\hat{\bar{\mathbf{E}}}_c^0, \quad \hat{\bar{\mathbf{E}}}_c^\eta = \mathbf{T}^0\hat{\bar{\mathbf{E}}}_c^\eta + \mathbf{T}^\eta\hat{\bar{\mathbf{E}}}_c^0, \quad \hat{\bar{\mathbf{E}}}_c^{\xi\eta} = \mathbf{T}^0\hat{\bar{\mathbf{E}}}_c^{\xi\eta} + \mathbf{T}^\xi\hat{\bar{\mathbf{E}}}_c^\eta + \mathbf{T}^\eta\hat{\bar{\mathbf{E}}}_c^\xi,\\
&\hat{\bar{\mathbf{E}}}_c^{\eta\zeta} = \mathbf{T}^0\hat{\bar{\mathbf{E}}}_c^{\eta\zeta} + \mathbf{T}^\eta\hat{\bar{\mathbf{E}}}_c^\zeta + \mathbf{T}^\zeta\hat{\bar{\mathbf{E}}}_c^\eta, \quad \hat{\bar{\mathbf{E}}}_c^{\zeta\xi} = \mathbf{T}^0\hat{\bar{\mathbf{E}}}_c^{\zeta\xi} + \mathbf{T}^\zeta\hat{\bar{\mathbf{E}}}_c^\xi + \mathbf{T}^\xi\hat{\bar{\mathbf{E}}}_c^\zeta
\end{aligned} \tag{7}$$

Thereby it should be noted that the terms of the product $(\mathbf{T}^0 + \xi\mathbf{T}^\xi + \eta\mathbf{T}^\eta + \zeta\mathbf{T}^\zeta)\hat{\bar{\mathbf{E}}}_c$ which depend on ξ^2,η^2,ζ^3 or $\xi\eta\zeta$ are omitted.

Split of enhanced strain. In the second place we look at the enhanced strain $\hat{\mathbf{E}}_e$. The paper of [32] contains a very simple interpolation of it reading

$$\hat{\mathbf{E}}_e = \hat{\mathbf{E}}_e^\star = \mathbf{T}^0\bar{\mathbf{B}}_e^\star W_e = \mathbf{B}_e^\star W_e \tag{8}$$

where W_e denotes the single enhanced degree-of-freedom. The matrix $\bar{\mathbf{B}}_e^\star = \{0,0,\zeta,0,0,0\}^T$ is chosen in such a way that the enhanced strain in thickness direction depends linearly on ζ. This is important to eliminate volumetric and Poisson thickness locking.

Computation of hourglass stress. It is now possible to compute the second term of (4). This is performed by stating

$$\frac{\partial \hat{\mathbf{E}}}{\partial \xi}\bigg|_{\boldsymbol{\xi}^\star}\xi = \hat{\mathbf{E}}_c^\xi\,\xi + \hat{\mathbf{E}}_c^{\zeta\xi}\,\zeta\,\xi, \quad \frac{\partial \hat{\mathbf{E}}}{\partial \eta}\bigg|_{\boldsymbol{\xi}^\star}\eta = \hat{\mathbf{E}}_c^\eta\,\eta + \hat{\mathbf{E}}_c^{\eta\zeta}\,\eta\,\zeta \tag{9}$$

We finally arrive at

$$\hat{\mathbf{S}}^{\mathrm{hg}} = \hat{\mathbf{C}}^{\mathrm{hg}} \left(\hat{\mathbf{E}}_c^{\xi}\, \xi + \hat{\mathbf{E}}_c^{\zeta\zeta}\, \zeta\, \xi + \hat{\mathbf{E}}_c^{\eta}\, \eta + \hat{\mathbf{E}}_c^{\eta\zeta}\, \eta\, \zeta \right) \tag{10}$$

This relation is linear in the local coordinates and in this way fulfills the requirement formulated at the beginning of Section 2.2.

Remark 1. The necessity to choose the parameter $\mu_{\mathrm{eff}}^{\mathrm{hg}}$ different from the shear modulus μ when plastic deformation is present is due to the fact that the hourglass stress (10) is computed on the basis of parts of the hourglass strain. Since the internal variables, among them the plastic strain, are evaluated only in the Gauss points, the hourglass strain does not undergo the split into elastic and plastic parts. Combining the original shear modulus with a total strain (the hourglass strain) obviously leads to too large values for $\hat{\mathbf{S}}^{\mathrm{hg}}$ and consequently locking. Thus, in order to obtain physically reasonable stress values the material stiffness in (10) has to be adapted accordingly. A suggestion to do that is found in [32] (n_{gp} number of Gauss points, ω_i weighting factor for Gauss point i):

$$\mu_{\mathrm{eff}}^{\mathrm{hg}} = \sum_{i=1}^{n_{gp}} \mu_i^{\mathrm{hg}}\, \omega_i = \sum_{i=1}^{n_{gp}} \left(\frac{1}{2} \sqrt{\frac{\mathbf{S}^{\star\,\mathrm{dev}} : \mathbf{S}^{\star\,\mathrm{dev}}}{\mathbf{E}^{\star\,\mathrm{dev}} : \mathbf{E}^{\star\,\mathrm{dev}}}} \right)_i \omega_i \tag{11}$$

Note that $\mathbf{S}^{\star\,\mathrm{dev}}$ and $\mathbf{E}^{\star\,\mathrm{dev}}$ are the deviatoric parts of the tensors $\mathbf{S}^{\star}$ and $\mathbf{E}^{\star}$, respectively.

2.3. Discretized weak form

As done in several earlier papers we use for the infinitesimal volume element $dV_e = J\, d\Omega^e$ the assumption $dV^e \approx J^0\, d\Omega^e$ ($d\Omega^e = d\xi\, d\eta\, d\zeta$). Here, J denotes the determinant of the Jacobian matrix $\mathbf{J} = \partial \mathbf{X} / \partial \boldsymbol{\xi}$. Replacing it by its value in the centre of the element ($J^0 = J|_{\xi=\eta=\zeta=0}$) means that the computation of the volume element is based on its equivalent parallelipiped instead of on the accurate shape of the hexahedron. Certainly this introduces an error into the analysis which, however, vanishes with increasing number of elements.

Inserting the expressions derived in Section 2.2 into Eq. (2) yields for each element ($\mathbf{U}_e$ element nodal displacement vector)

$$g_2^e = \int_{\Omega^e} \delta \hat{\mathbf{E}}_e^T\, \hat{\mathbf{S}} J^0\, d\Omega^e = \int_{\Omega^e} (\delta \hat{\mathbf{E}}_e^{\star})^T\, \hat{\mathbf{S}}^{\star} J^0\, d\Omega^e = \delta W_e \int_{\Omega^e} (\mathbf{B}_e^{\star})^T\, \hat{\mathbf{S}}^{\star} J^0\, d\Omega^e = \delta W_e \underbrace{\int_{\zeta=-1}^{1} (\mathbf{B}_e^{\star})^T\, \hat{\mathbf{S}}^{\star}\, d\zeta\, 4 J^0}_{R_W(\mathbf{U}_e, W_e)} = 0 \tag{12}$$

Due to the inter element discontinuity of the enhanced strain $\hat{\mathbf{E}}_e$ this equation has to be fulfilled for each element.

Concerning the element part of g_1 in (1), we are mainly interested in rewriting the first term. We obtain

$$\begin{aligned} \int_{\Omega^e} \delta \hat{\mathbf{E}}_c^T\, \hat{\mathbf{S}} J^0\, d\Omega^e &= \int_{\Omega^e} (\delta \hat{\mathbf{E}}_c^{\star})^T\, \hat{\mathbf{S}}^{\star} J^0\, d\Omega^e + \int_{\Omega^e} (\delta \hat{\mathbf{E}}_c^{\mathrm{hg}})^T\, \hat{\mathbf{S}}^{\mathrm{hg}} J^0\, d\Omega^e + \underbrace{\int_{\Omega^e} (\delta \hat{\mathbf{E}}_c^{\star})^T\, \hat{\mathbf{S}}^{\mathrm{hg}} J^0\, d\Omega^e}_{=0} + \underbrace{\int_{\Omega^e} (\delta \hat{\mathbf{E}}_c^{\mathrm{hg}})^T\, \hat{\mathbf{S}}^{\star} J^0\, d\Omega^e}_{=0} \\ &= \delta \mathbf{U}_e^T (\mathbf{R}_u^{\star} + \mathbf{R}_u^{\mathrm{hg}}) \end{aligned} \tag{13}$$

For the variations $\delta \hat{\mathbf{E}}_c^{\bullet}$ and $\delta \hat{\mathbf{E}}_c^{\bullet\bullet}$ ($\bullet = \xi, \eta, \zeta$) included in $\delta \hat{\mathbf{E}}_c^{\star}$ as well as in $\delta \hat{\mathbf{E}}_c^{\mathrm{hg}}$ we introduce the corresponding "**B**" matrices according to $\delta \hat{\mathbf{E}}_c^{\bullet} = \mathbf{B}_c^{\bullet}\, \delta \mathbf{U}_e$ and $\delta \hat{\mathbf{E}}_c^{\bullet\bullet} = \mathbf{B}_c^{\bullet\bullet}\, \delta \mathbf{U}_e$. The matrices $\mathbf{B}_c^{\bullet}$ and $\mathbf{B}_c^{\bullet\bullet}$ do not depend on the local coordinates. The internal force vector $\mathbf{R}_u^{\star}$ results from the first term of (13) and reads in detail:

$$\mathbf{R}_u^{\star} = \int_{\zeta=-1}^{1} (\mathbf{B}_c^0 + \zeta\, \mathbf{B}_c^{\zeta} + \zeta^2\, \mathbf{B}_c^{\zeta\zeta})^T\, \hat{\mathbf{S}}^{\star}\, d\zeta\, 4 J^0 \tag{14}$$

Due to the non-linear and unknown dependence of $\hat{\mathbf{S}}^{\star}$ on ζ the evaluation of $\mathbf{R}_u^{\star}$ requires a numerical integration over ζ. In contrast to a full integration with two Gauss points in ξ-, η- and ζ-direction we reduce the number of Gauss points to one fourth. In the context of explicit methods this ratio is equivalent to the gain in computational effort, since the CPU time for the solution of the global finite element system is proportional to the number of Gauss points.

A small additional computational effort is generated by the calculation of the second part of the internal force vector

$$\mathbf{R}_u^{\mathrm{hg}} = \left(\frac{8}{3} (\mathbf{B}_c^{\xi})^T\, \hat{\mathbf{C}}^{\mathrm{hg}}\, \hat{\mathbf{E}}_c^{\xi} + \frac{8}{3} (\mathbf{B}_c^{\eta})^T\, \hat{\mathbf{C}}^{\mathrm{hg}}\, \hat{\mathbf{E}}_c^{\eta} + \frac{8}{9} (\mathbf{B}_c^{\zeta\xi})^T\, \hat{\mathbf{C}}^{\mathrm{hg}}\, \hat{\mathbf{E}}_c^{\zeta\xi} + \frac{8}{9} (\mathbf{B}_c^{\xi\eta})^T\, \hat{\mathbf{C}}^{\mathrm{hg}}\, \hat{\mathbf{E}}_c^{\xi\eta} \right) J^0 \tag{15}$$

which does not require any numerical integration.

After assembly and implementation of the boundary conditions we finally arrive at the equation

$${}^{G}\mathbf{G} = {}^{G}\mathbf{R}_u^{\star} + {}^{G}\mathbf{R}_u^{\mathrm{hg}} + {}^{G}\mathbf{D}\, {}^{G}\dot{\mathbf{U}} + {}^{G}\mathbf{M}\, {}^{G}\ddot{\mathbf{U}} - {}^{G}\mathbf{P}_{\mathrm{ext}} = \mathbf{0} \tag{16}$$

where the index G indicates finite element matrices and vectors defined at the global finite element level. Further, ${}^{G}\mathbf{D}$ is the global damping matrix, ${}^{G}\mathbf{M}$ the global mass matrix and ${}^{G}\mathbf{P}_{\text{ext}}$ the global load vector. In most simulations we neglect damping. If we do not do so it is explicitly stated.

In explicit analyses, the nodal accelerations are computed from (16) at each step by inverting the diagonal mass matrix. Nodal velocities and displacements are then obtained by explicit time integration. At each time step and for each element, one is therefore required to compute the internal nodal forces $\mathbf{R}_u^{\star}$, $\mathbf{R}_u^{\text{hg}}$ and the enhanced strain parameter W_e for assigned nodal displacements. For nonlinear material behavior, $\hat{\mathbf{S}}^{\star}$ in (12) depends nonlinearly on W_e and one has to solve iteratively a nonlinear implicit problem for each time step (see e.g. [20]), involving for each iteration the integration of the constitutive behavior at all Gauss points. Even in the present case of reduced integration with only one enhanced strain parameter per element, this iterative process carried out at each time step and involving all element Gauss points may become critical in terms of computing time when the time step size is very small, as it happens in most cases in explicit dynamics simulations.

As a possible remedy, one can consider the possibility to keep the current value of W_e fixed, carrying out its update only after a certain number of time steps. Of course this implies an error in Eq. (12), which increases with the number of time steps between two subsequent updates. Another possibility, consistent with the explicit character of the adopted time integration, consists of computing at each time step an explicit estimate of the increment ΔW_e by linearizing Eq. (12) with respect to W_e. While in the general case R_W in (12) is a function also of $\mathbf{U}_e$, for the computation of the explicit estimate of ΔW_e the nodal displacements have to be regarded as prescribed and the linearization has to be carried out only with respect to W_e, obtaining

$$\Delta W_e = -S_{WW}^{-1} R_W, \quad S_{WW} = \int_{\zeta=-1}^{1} (\mathbf{B}_e^{\star})^T \hat{\mathbf{C}}^{\star} \mathbf{B}_e^{\star} \, d\zeta 4J^0 \tag{17}$$

The residual R_W is computed using the stress $\hat{\mathbf{S}}^{\star}$ obtained from the constitutive update carried out at the Gauss points. The expression $S_{WW} = \partial R_W / \partial W_e$ represents the tangent of the residual, with $\hat{\mathbf{C}}^{\star}$ being the matrix of material tangent moduli evaluated at the Gauss points. The explicit estimate of W_e obtained in this way is to be used in the next step for the constitutive update. This explicit computation is rather inexpensive, the most time consuming part being represented by the construction of the matrix of tangent moduli $\hat{\mathbf{C}}^{\star}$, which would not be required otherwise. The two alternative provisions will be comparatively investigated through numerical tests in Section 3.

3. Selective mass scaling

As discussed in several papers (e.g. Mattern et al. [24] and Pagani et al. [30]) the disadvantage of using solid-shell finite element formulations in combination with explicit methods is the small critical time step determined by the thickness of the structure. Note that classical four-node shell formulations do not suffer from this problem because they allow to compute the critical time step on the basis of the smallest element dimension in the shell plane. Clearly, in most cases, this dimension is much larger than the thickness. Among the methods to increase the critical time step, the strategy of selective mass scaling has attracted noticeable attention. We follow here the method of Cocchetti et al. [9] and Pagani et al. [30] which can be summarized as follows.

Standard mass scaling means to work with an artificially increased density (mass pumping) which certainly allows to work with a larger critical time step. However, it is obvious and well-known that this procedure might noticeably influence the dynamic behaviour of a structure. A more sophisticated idea is to design the mass scaling such that only the higher order structural eigenmodes are affected. These are the ones which determine the critical time step whereas the overall dynamic behaviour is rather controlled by the low order structural eigenmodes. Thus, a so-called selective mass scaling procedure which influences the higher order modes (e.g. relative movements between the upper and the lower surface of a solid-shell element) but retains the low order ones (e.g. the element rigid body translations) is promising in the regard that the critical time steps can be increased without changing the main characteristics of the dynamic structural behaviour.

To split between low and high order modes we split the 8-node element vector of nodal accelerations $\mathbf{A}_e := \ddot{\mathbf{U}}_e$ ($\mathbf{U}_e$ element vector of nodal displacements) into the two parts (12×1 vectors)

$$\mathbf{A}_e^{\text{ave}} = \frac{1}{2} [\mathbf{I} \quad \mathbf{I}] \mathbf{A}_e \text{ and } \mathbf{A}_e^{\text{diff}} = \frac{1}{2} [-\mathbf{I} \quad \mathbf{I}] \mathbf{A}_e \tag{18}$$

where $\mathbf{A}_e^{\text{ave}}$ represents rigid body translations and $\mathbf{A}_e^{\text{diff}}$ relative movements. The 12×12 matrix $\mathbf{I}$ is an identity matrix. The 24×1 vector $\mathbf{A}_e$ contains on the first 12 positions the accelerations in the three coordinate directions of the nodes 1 to 4, i.e. the nodes of the lower solid-shell surface. The last 12 positions are filled with the corresponding accelerations of the upper solid-shell surface (nodes 5 to 8). Defining the 24×1 vector $\tilde{\mathbf{A}}_e$ by $\tilde{\mathbf{A}}_e^T = \{(\mathbf{A}_e^{\text{ave}})^T (\mathbf{A}_e^{\text{diff}})^T\}$ we arrive at the mapping

$$\mathbf{A}_e = \mathbf{T}_{ms} \tilde{\mathbf{A}}_e \text{ with } \mathbf{T}_{ms} = \begin{bmatrix} \mathbf{I} & -\mathbf{I} \\ \mathbf{I} & \mathbf{I} \end{bmatrix} \tag{19}$$

Transforming the balance of linear momentum at the element level accordingly leads to the equation

$$\underbrace{\mathbf{T}_{ms}^{T}\mathbf{M}_{e}\mathbf{T}_{ms}}_{\tilde{\mathbf{M}}_{e}}\tilde{\mathbf{A}}_{e}=\underbrace{\mathbf{T}_{ms}^{T}\left(\mathbf{P}_{\text{ext}}-\mathbf{R}_{u}\right)}_{\tilde{\mathbf{P}}_{\text{ext}}-\tilde{\mathbf{R}}_{u}} \tag{20}$$

where $\mathbf{R}_u = \mathbf{R}_u^{\star} + \mathbf{R}_u^{\text{hg}}$ holds and $\mathbf{P}_{\text{ext}}$ denotes the element contribution of the external loading.

For the present solid-shell formulation, the mass matrix $\mathbf{M}_e$ takes after lumping the form

$$\mathbf{M}_{e}=\rho J^{0}\begin{bmatrix}\mathbf{I} & \mathbf{0}\\ \mathbf{0} & \mathbf{I}\end{bmatrix} \tag{21}$$

In this case, the transformation (20) retains the diagonal form so that we obtain $\tilde{\mathbf{M}}_e = 2\,\mathbf{M}_e$. The idea of the present selective mass scaling is to change the components of the mass matrix $\tilde{\mathbf{M}}_e$ correlated with the higher order modes contained in $\tilde{\mathbf{A}}_e^{\text{diff}}$:

$$\tilde{\mathbf{M}}_{e}=2\,\rho J^{0}\begin{bmatrix}\mathbf{I} & \mathbf{0}\\ \mathbf{0} & \beta\mathbf{I}\end{bmatrix} \tag{22}$$

An optimum choice of the factor β can be found by studying the eigenfrequencies at the element level. The factor β should lower the eigenfrequencies of the higher order modes in such a way that they are of the same order as the low order modes. In this way the disadvantage of working with solid-shell formulations in explicit simulations can be overcome because the thickness dimension no longer dictates the critical time step.

An additional problem is given by the computation of the critical time step size, which depends on the maximum eigenfrequency of the scaled element. The estimates which are usually employed in elements with uniform density are of no use after the masses have been selectively scaled. In the applications, the analytical estimate proposed in [9], which is applicable to regular parallelepiped or slightly distorted elements, has been used.

The estimate of the critical time step size is based on the fact that in solid-shell elements, where the thickness dimension is significantly smaller than the in-plane ones, the highest element eigenfrequency ω_{max} always turns out to be given by the square root of the eigenvalue corresponding to the thickness vibration mode (see e.g. [11]). In the case of a regular parallelepiped, in [9] it has been shown that the critical time step resulting from this eigenfrequency is given by

$$\Delta t=\frac{2}{\omega}=24\sqrt{\frac{ab\rho(1+\nu)}{\eta E}} \tag{23}$$

a and b being the element in-plane semi-dimensions, ν the Poisson coefficient, ρ the material density and E the Young modulus. The parameter η is a function of the mass scaling parameter and is computed as the largest root of the non-dimensional cubic equation

$$\beta\gamma^{2}\lambda^{2}(1-2\nu)\eta^{3}-144\gamma\lambda[1+\beta(\gamma^{2}+\lambda^{2})](1-\nu)\eta^{2}+144^{2}(\lambda^{2}+\gamma^{2}+\beta\gamma^{2}\lambda^{2})\eta-144^{3}\gamma\lambda(1+\nu)=0 \tag{24}$$

resulting from the element eigenvalue problem governing the thickness eigenmode. The coefficients γ and λ are defined as $\gamma = c/a, \lambda = c/b$, where c is the half-thickness.

The scaling parameter β has to be optimized so as to maximize the time step size without significant accuracy losses. For high values of β, the critical time step Δt in (23) exhibits an asymptote (see Fig. 1), which means that the eigenfrequency corresponding to the thickness vibration mode has decreased to the point that the critical time step size becomes determined by the in-plane traversal time and not anymore by the element thickness. Higher values of β would hence be useless,

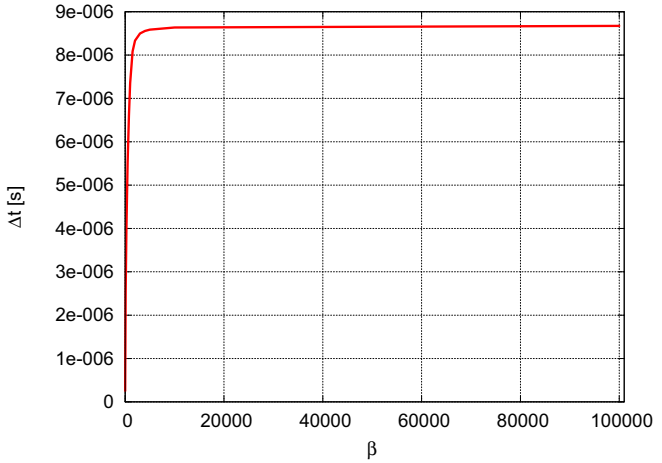

Fig. 1. Trend of Δt for varying value of β.

since they would not bring an increase of the critical time step, while leading to inaccurate solutions. A possible strategy for the determination of the optimal value of β consists first in the determination of the asymptotic value Δt^{asy} of the critical time step, which can be computed letting $\beta \to \infty$ in (24). In this way, the following quadratic equation is obtained:

$$\gamma^2\lambda^2(1-2\nu)\eta^3 - 144\gamma\lambda(\gamma^2+\lambda^2)(1-\nu)\eta^2 + 144^2\gamma^2\lambda^2\eta = 0. \tag{25}$$

The root of interest of(25) is given by

$$\eta^{asy} = \frac{72\left[(\gamma^2+\lambda^2)(1-\nu)+\sqrt{\Delta}\right]}{\gamma\lambda(1-2\nu)} \tag{26}$$

with $\Delta = (1-\nu)^2(\gamma^4+\lambda^4) + 2(\nu^2+2\nu-1)\gamma^2\lambda^2$. The corresponding asymptotic value of the critical time step Δt^{asy} is then given by

$$\Delta t^{asy} = 24\sqrt{\frac{ab\rho(1+\nu)}{E\eta^{asy}}} \tag{27}$$

As a trade-off between accuracy and computational efficiency, the optimal value β^{opt} of the scaling parameter is chosen as the one which produces an estimate of the critical time step equal to $0.9\Delta t^{asy}$, since values of β higher than this limit produce only a limited increase of the time step at the cost however of possible accuracy loss. The value of β to be used for mass scaling is then obtained by solving for β equation (24), which is linear in β, after setting $\eta = \eta^{asy}/(0.9)^2$, which corresponds to $\Delta t = 0.9\Delta t^{asy}$ in (23).

4. Numerical examples

We illustrate the performance of the Q1STs element in the explicit framework by means of several examples.

4.1. Impulsively loaded cantilever

4.1.1. Linear-elastic case

A cantilever beam is used to study the linear-elastic response of the Q1STs element. Working with the original (implicit) version of the Q1STs formulation means that the internal element degrees-of-freedom (related to the EAS concept) as well as the hourglass stabilization have to be updated in every time step. In the context of explicit integration characterized by extremely small time steps this is computationally not efficient. Therefore, in this example we investigate whether carrying out this update in only each (nS)th (hourglass stabilization) or (nE)th (EAS degrees-of-freedom) time step, or computing at each time step an explicit estimate (hereafter denoted as *expEAS*) of the EAS degrees of freedom, as discussed in Section 1, alters the solution and reduces the computational effort. If not otherwise stated $nS = 1$ holds when nE is varied and $nE = 1$ holds when nS is varied. On the other hand, when the *expEAS* strategy is adopted, the explicit estimate is carried out at each time step, while the implicit update of the EAS degrees of freedom is never carried out ($nE = \infty$) and the hourglass stabilization is updated at each time step ($nS = 1$). In general we work with a time step of $\Delta t = 1.4 \cdot 10^{-5}$ s.

The beam depicted in Fig. 2 has a side length of $l = 6000$ mm and a rectangular cross section of $w = 200$ mm multiplied with $h = 100$ mm. The cantilever is made of steel. The material parameters are given by $E = 200000$ N/mm^2 (Young's modulus), $\nu = 0.3$ (Poisson's ratio) and $\rho = 7.5 \cdot 10^{-9}$ Ns^2/mm^4 (mass density). A constant concentrated tip load $F = 500$ N is applied in vertical direction. It is equally distributed among the four nodes of the tip. We compute the displacement at the bottom row of nodes at the tip. The analytical static solution is $v_{\text{ref}} = 10.8$ mm. The structure is discretized by either 6 or 12 elements over the length l. In the other two directions only one element is used.

For the six elements mesh, Fig. 3(a) shows that the influence of nS on the solution is negligible. For $nS > 100$ the CPU time drops by about 12.5%. This percentage cannot be increased further which can be explained as follows. Let us assume that the CPU effort $T_1 = aT_1 + (1-a)T_1$ for a time step with update can be split into two parts. The first summand (aT_1) relates to the time invested on the update of the hourglass stabilization. The second summand represents the CPU time needed for all other operations within the element for one time step. For a time step without update we have simply $T_2 = (1-a)T_1$. We assume that n_{tot} time steps are computed and obtain for the total CPU effort $T_{\text{tot}} = b\,n_{\text{tot}}\,T_1 + (1-b)\,n_{\text{tot}}\,(1-a)\,T_1$. In the latter formula $100b\,\%$ denotes the percentage of the time steps with update. In the limit of $b \to 0$ (no update) the total

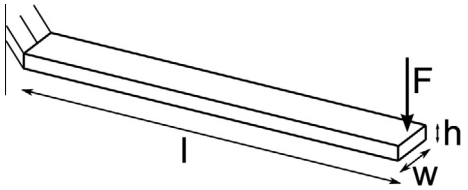

Fig. 2. Cantilever beam. Geometry and boundary conditions.

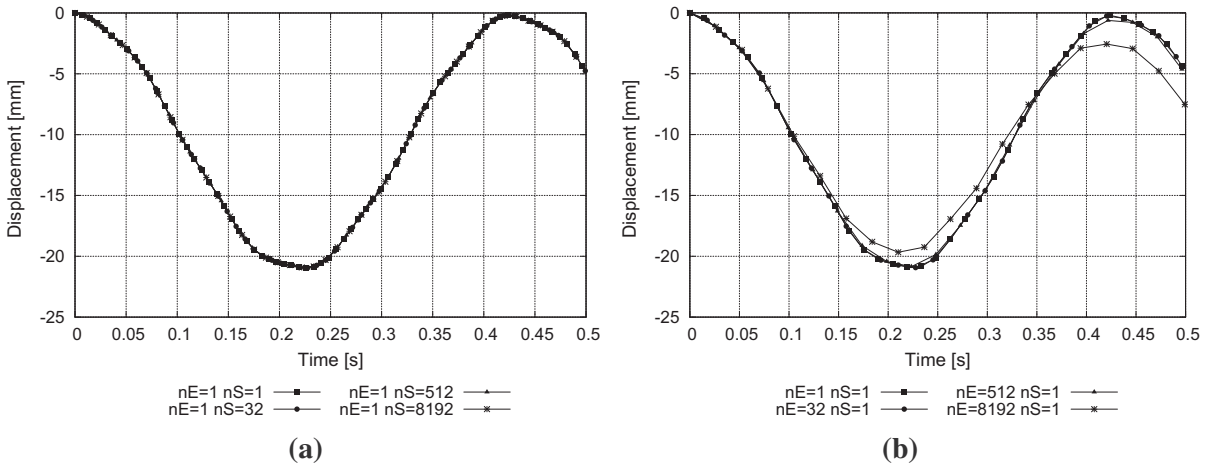

Fig. 3. Tip displacement of linear-elastic cantilever beam (6 elements mesh). (a) Dependence on *nS*, (b) Dependence on *nE*.

CPU time amounts to $(T_{\text{tot}})_{b\to 0} = n_{\text{tot}}(1-a)T_1$. For $b = 1$ (update in every time step) the result is $(T_{\text{tot}})_{b=1} = n_{\text{tot}}T_1$. Thus, the ratio $(T_{\text{tot}})_{b\to 0}/(T_{\text{tot}})_{b=1}$ takes on the maximum value $1-a$. This means the reduction of the total CPU effort is only controlled by the difference in CPU time between a time step with and without update. Consequently, the computational effort in the element devoted to the update of the hourglass stabilization amounts to about 12.5%.

Updating the internal element degree-of-freedom only every *nE*th time step has a noticeable effect on the solution (see Fig. 3b). But also the reduction of the CPU effort is larger (about 19.7% in the case $nE = 8192$). Finally, the *expEAS* strategy (see Fig. 4) does not produce any visible effect on the response while allowing for a reduction of 18.7% of CPU time. It should be noted that even in this linear elastic case, the explicit estimate of the enhanced strain parameter brings a non-negligible computational gain. This is due to the fact that in this way the enhanced strain parameter to be used in the next step is estimated at the element level in the same loop of the internal force vector, which is computed making use of the parameter estimate coming from the previous step, without the need of an additional loop over the element Gauss points.

Using the same argument as above we can conclude that the computational effort in the element to compute the internal element degree-of-freedom exceeds the CPU time for the update of the hourglass stabilization. This time is expected to increase when an elastoplastic response is considered.

Explicit methods are obviously well suited for dynamic problems. However, often one is rather interested in the quasi-static response. The latter is more easily accessible if damping is included. Among the several possibilities to achieve that, we choose one of the simplest. The damping matrix $\mathbf{D}_e$ (element contribution of ${}^{G}\mathbf{D}$) is assumed to read $\mathbf{D}_e = \alpha \mathbf{M}_e$. In this way, it has also diagonal form and does not increase the computational effort in the explicit integration. However, a disadvantage of this procedure is the necessity to choose the parameter α with the dimension $[s^{-1}]$. It represents the ratio between the viscosity per square meter and the density. As such it is related in some way to the geometry of the structure which

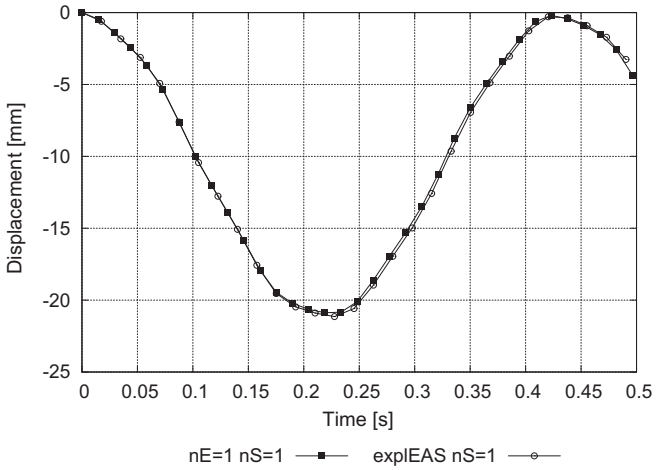

Fig. 4. Tip displacement of linear-elastic cantilever beam (6 elements mesh): *expEAS* strategy.

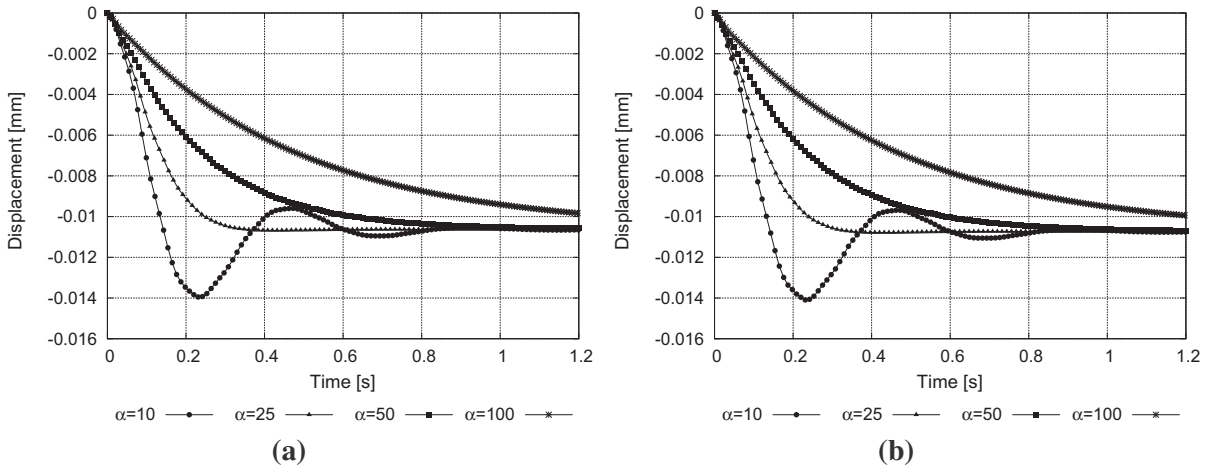

Fig. 5. Quasistatic behavior of linear-elastic cantilever. (a) 6 elements (b) 12 elements.

means that the influence of the damping introduced in this way is not only material- but also geometry-dependent. In the present example the choice $\alpha = 50\ s^{-1}$ lets us most quickly reach the quasi-static solution (see Fig. 5). This holds for both discretizations (6 and 12 elements). Thus, the effect of α might be geometry-dependent but is not influenced by the finite element discretization.

To test the capability of the proposed selective mass scaling technique in the very thin limit, the previously described beam problem with the 6 elements mesh has been tested considering different thicknesses: $h = 100, h = 50, h = 25, h = 10$ mm. With the thickness $h = 10$ mm, the element width to thickness ratio is $w/h = 20$. To remain in the linear, small displacement range for all thicknesses and to obtain comparable curves, the applied load has been scaled in each case so as to obtain the same static tip displacement: $F = 500, F = 62.5, F = 7.8125, F = 0.5$ N.

For each thickness, the new procedure illustrated in Section 2 provides in an automatic way the optimal value of the mass scaling parameter, so that the stable time step Δt is 90% of Δt^{asy}. From Table 1 one can see that, as expected, the obtained stable time step is the same for all thicknesses and therefore is no longer dictated by the element thickness. The gain with respect to the case of unscaled masses (see the columns "Δt" and "$\Delta t\ (\beta = 1)$") grows as the thickness decreases and is almost equal to the element aspect ratio (width to thickness ratio w/h in this case). In particular, the gain amounts to more than one order of magnitude in the thinnest case. On the other hand, the accuracy loss is negligible. Fig. 6(a) shows the curves obtained for the different thicknesses. As expected, the beam first eigenperiod increases linearly with the thickness reduction. This aspect, which confirms that the structural dynamic response is not compromised by the growing mass scaling factor, can be better appreciated in Fig. 6(b), where the same curves are plotted against a time scaled by the beam first eigenperiod T. One can notice that the curves are perfectly superposed and no effects of the scaling can be observed.

To further test the effect of mass scaling on the results accuracy, the thinnest beam ($h = 10$ mm) has been tested with increasing values of the mass scaling parameter β (Fig. 7). As shown in Table 2, the gain in the time step size becomes negligible for values of β larger than the one suggested by the adopted strategy, while the accuracy quickly deteriorates.

4.1.2. Non-linear case

In the following section we study the non-linear behaviour of the cantilever beam considered in the previous example. For this purpose we consider a perfectly elasto-plastic model with a yield stress of 250 N/mm^2. The other material parameters are the same as in Section 4.1.1 A concentrated tip load $F = 16000$ N is applied in the vertical direction. Again, the vertical displacement v at the lower row of nodes at the tip is investigated. The beam is discretized by means of 30 elements over the length and one element in the other two directions. Five Gauss points are used in the thickness direction. Without mass scaling, the stable time step is $\Delta t = 1.58 \cdot 10^{-5}$ s. The influence of nS and nE on the solution is now much more significant (see Fig. 8). A relative error e in the tip displacement v

Table 1
Linear elastic cantilever: optimal mass scaling parameter β and stable time step for increasing beam thickness.

h	β	Δt	$\Delta t(\beta = 1)$	$\Delta t/\Delta t(\beta = 1)$	w/h
10	579	2.99E−5	1.67E−6	17.90	20
25	93	2.99E−5	4.17E−6	7.17	8
50	23	2.99E−5	8.29E−6	3.60	4
100	5.78	2.99E−5	1.62E−5	1.84	2

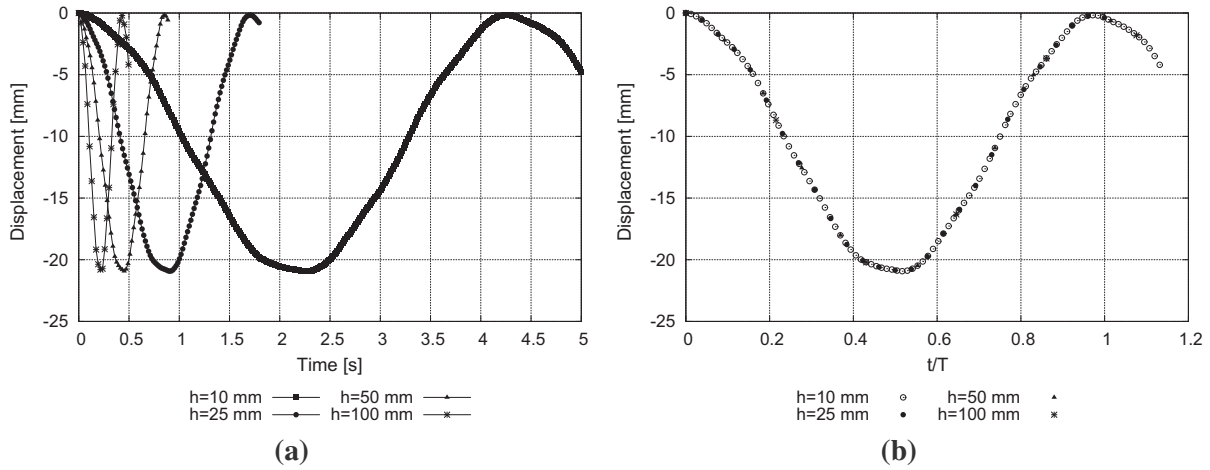

Fig. 6. Linear-elastic cantilever beam with varying thickness and selective mass scaling. (a) Tip displacement for varying thickness and mass scaling. (b) Same as (a) with scaled time. Mass scaling parameters values are reported in Table 1.

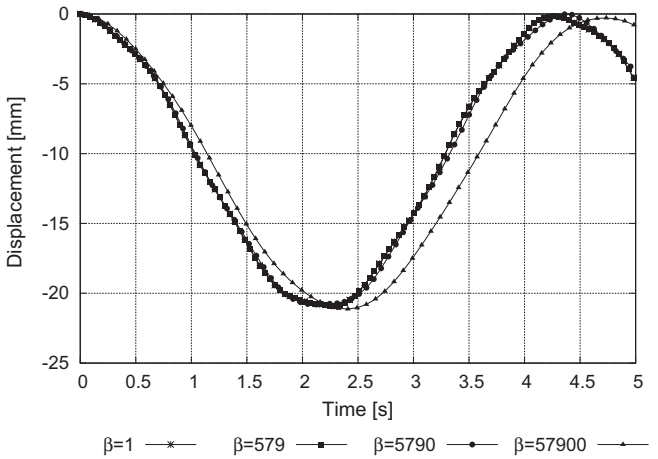

Fig. 7. Linear elastic cantilever: response for increasing value of mass scaling parameter; thickness $h = 10$ mm.

Table 2
Linear elastic cantilever: stable time step for increasing mass scaling.

β	Δt
1	1.67E−6
579	2.99E−5
5790	3.30E−5
579000	3.32E−5

$$e = \frac{v_{nS} - v_{nS=1}}{v_{nS=1}} 100\%$$

of about 10% is reached for $nS = 10000$. In the computation where nE is varied we arrive at a maximum error of about 33% which is certainly not acceptable. Nevertheless, the large influence carries over to the CPU time. Working with $nE = 10000$ lets us reduce the computational effort by about 64% (see Table 3). The adoption of the *expEAS* strategy does not produce any visible error in the tip displacement and also reduces the CPU time by about 63%. For $nS = 10000$ we reach a gain in CPU time of again 12.5 %. This leads us to the conclusion that the amount of CPU time invested in the update of the hourglass stabilization at the element level does not depend on the degree of non-linearity of the analysis. The situation is very different in the context of the enhanced strain method which in the non-linear case requires much more computational effort than in linear elasticity.

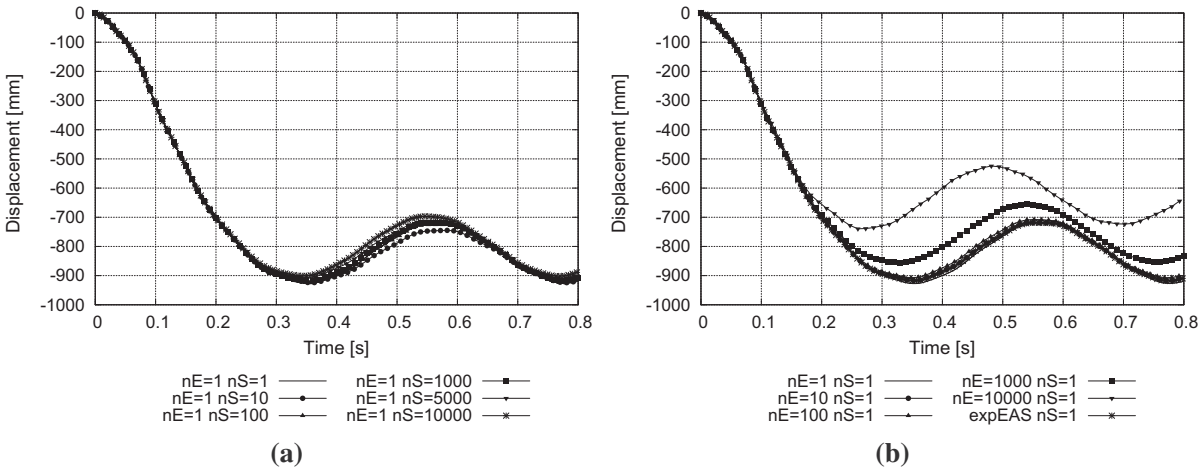

Fig. 8. Tip displacement of elastoplastic cantilever beam (30 elements mesh). (a) Dependence on *nS*, (b) Dependence on *nE*.

Table 3
CPU time nonlinear cantilever beam.

nS	CPU time [s]	*nE*	CPU time [s]
1	1267.34	1	1267.34
10	1193.29	10	541.17
100	1189.12	100	468.66
1000	1183.73	1000	462.69
5000	1181.58	5000	461.03
10000	1182.88	10000	458.38

Explicit simulation in the context of elastoplastic material behaviour is more difficult because plastic strain accumulates in each oscillation. The solution reached after the system has come to a rest therefore depends on the number of oscillations which have taken place before. This is also seen in Fig. 9(a). The solution for $\alpha = 100\ s^{-1}$ is the stiffest one because due to the rather high damping the systems react slowly. Thus, less plastic strain accumulates. The solutions for $\alpha = 50\ s^{-1}$ and $\alpha = 30\ s^{-1}$ are similar. In contrast to the curve for $\alpha = 100\ s^{-1}$ one observes two inflection points at the beginning (see Fig. 9(b)). After that, the absolute value of the displacement increases until a horizontal tangent is reached. For $\alpha = 10\ s^{-1}$ the inflection points are more pronounced. Further inflection points are found (one oscillation) before an approximately horizontal tangent is obtained. Due to this oscillation more plastic strain accumulates which changes the converged solution.

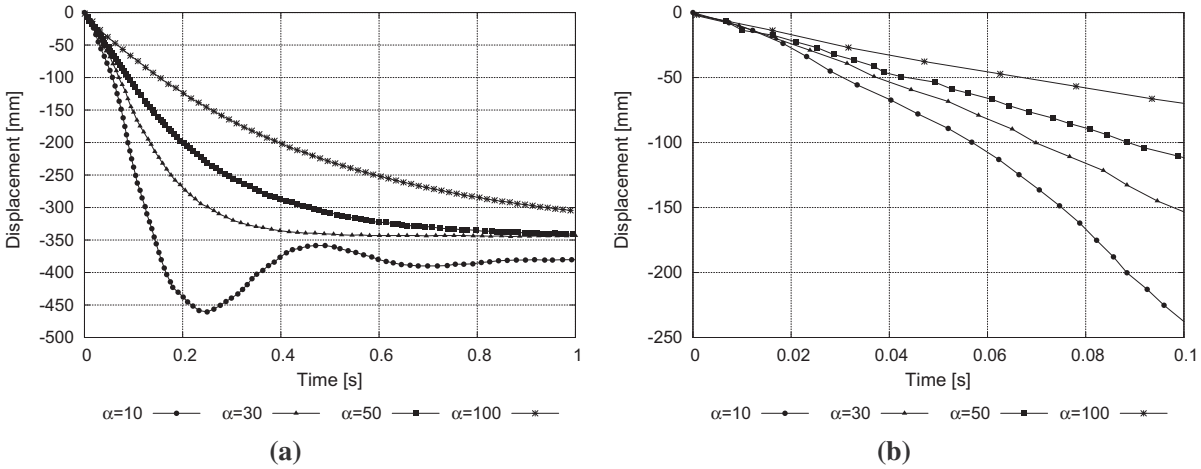

Fig. 9. Quasi-static behaviour of elasto-plastic cantilever. (a) Full range, (b) Range from 0 to 0.1 s.

In summary, we have four methods available to reduce the computational effort of the explicit analysis:

(1) Updating the hourglass stabilization only every nS time step.
(2) Updating the internal element dofs (enhanced strain method) at only every nEth time step.
(3) Explicitly updating the internal elements dofs at each time step (*expEAS*).
(4) Selective mass scaling.

The responses obtained for the elastoplastic cantilever beam with the 6 and 30 elements meshes, using different combinations of these methods, are shown in Fig. 10. The optimal selective mass scaling coefficient $\beta = 5.78$ is obtained using the procedure illustrated in Section 2 for the 6 elements mesh and $\beta = 4.75$ for the 30 elements mesh. The two values are very close because in both meshes the elements have a minimum in-plane-dimension/thickness ratio equal to 2. Since the difference is small, a common value $\beta = 5$ is used in both cases to obtain comparable curves. The standard is using $nS = nE = 1$ and $\beta = 1$. This means to update the hourglass stabilization and the internal element dofs in every time step. The choice $\beta = 1$ implies that selective mass scaling is not switched on. For this computation we have a CPU effort of 257.33 s (6 elements) and 1267.34 s (30 elements). Note that these values are used only as reference. They could be certainly reduced by using more advanced hardware. The ratio between these two numbers (≈ 5) confirms that the CPU effort in an explicit analysis is more or less proportional to the number of elements. For the discretization with 6 elements, the choice of $nS = 1000$ leads to a noticeable deviation of the results. It is therefore suitable to work either with $nS = nE = 100$ or with $nS = 100$ and to adopt the *expEAS* strategy. The use of selective mass scaling with $\beta = 5$ enables the use of the time steps $\Delta t = 2.92 \cdot 10^{-5}$ s for 6 elements (instead of $1.62 \cdot 10^{-5}$ s, corresponding to $\beta = 1$) and $\Delta t = 2.53 \cdot 10^{-5}$ s for 30 elements (instead of $1.58 \cdot 10^{-5}$ s), without any noticeable accuracy loss. It should be noted that even though the same mass scaling has been used for the two meshes, a slightly different stable time step has been obtained in the two cases, since different elements exhibit a different maximum eigenfrequency. With these values, for 6 elements we obtain a CPU time of 26.25 s, while for 30 elements the CPU time is finally reduced to 130.47 s. This is for both discretizations a reduction to only approximately 10% of the original CPU effort.

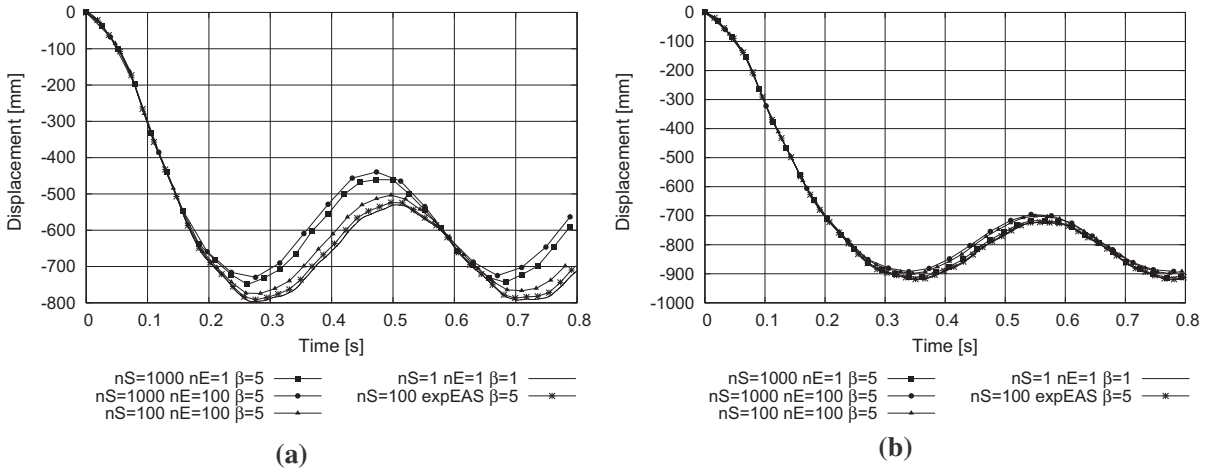

Fig. 10. Different techniques to compute elasto-plastic cantilever. (a) 6 elements, (b) 30 elements.

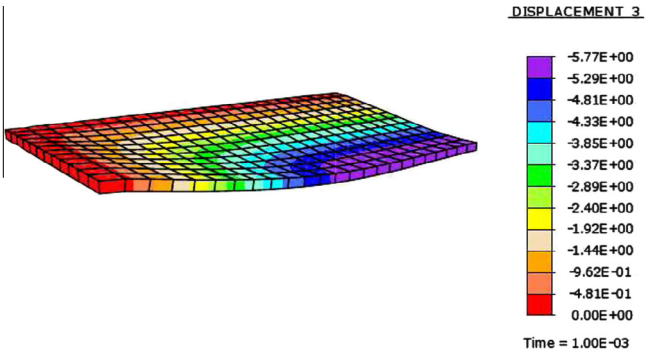

Fig. 11. Explosively loaded rectangular panel. Vertical displacement contour.

4.2. Explosively loaded rectangular panel

A rectangular shell panel, firmly clamped on all four sides, is exposed to the detonation of a high explosive layer. The problem illustrates the use of initial velocity conditions to model impulsive loadings arising from a detonation (Fig. 11). The geometry of the panel surface is given by the dimensions 76 mm and 130 mm. The thickness of the panel is equal to 1.5 mm. Due to the symmetry of the system only one quarter of the panel is discretized. Clamped boundary conditions are prescribed on two edges of the model, while the appropriate symmetry conditions are imposed along the remaining edges. The shell is made of steel. The Young's modulus is equal to 200,000 MPa, the Poisson's ratio is 0.3, and the density amounts to $7.5 \cdot 10^{-9}$ Ns^2/mm^4. A perfectly elastoplastic material model is employed with a yield stress of 250 MPa. A mesh of $12 \times 24 \times 1$ solid-shell elements is used. The load produced by the explosion is simulated by prescribing a uniform initial velocity of 35,000 mm/s to the nodes of the plate. The stable time step is $2.35 \cdot 10^{-7}$ s.

Choosing $nS = 100$ does not produce any visible effect on the solution (see Fig. 12(a)). Also the CPU time can hardly be reduced. The situation is different when the update of the internal element degree-of-freedom is performed only every nE steps. The choice $nE = 100$ reduces the oscillating displacement by more than 10% (Fig. 12(b)). The results obtained using $nS = 1, nE = 1$, optimal selective mass scaling $\beta = 4.36$ (providing a stable time step of $3.63 \cdot 10^{-7}$ s) and explicit estimate of the enhanced strain parameter (*expEAS*) are shown in Fig. 13. Almost no difference in the response curves can be appreciated, while the computation time can be still reduced to 26.6% of the original time.

The plate clamping on the four sides represents a highly constrained kinematic condition, which makes the development of hourglass modes difficult. In this respect, a more challenging test is obtained by simply supporting the plate on the four corners [2] and applying a uniform pressure equal to 1 MPa. The displaced configurations obtained without and with

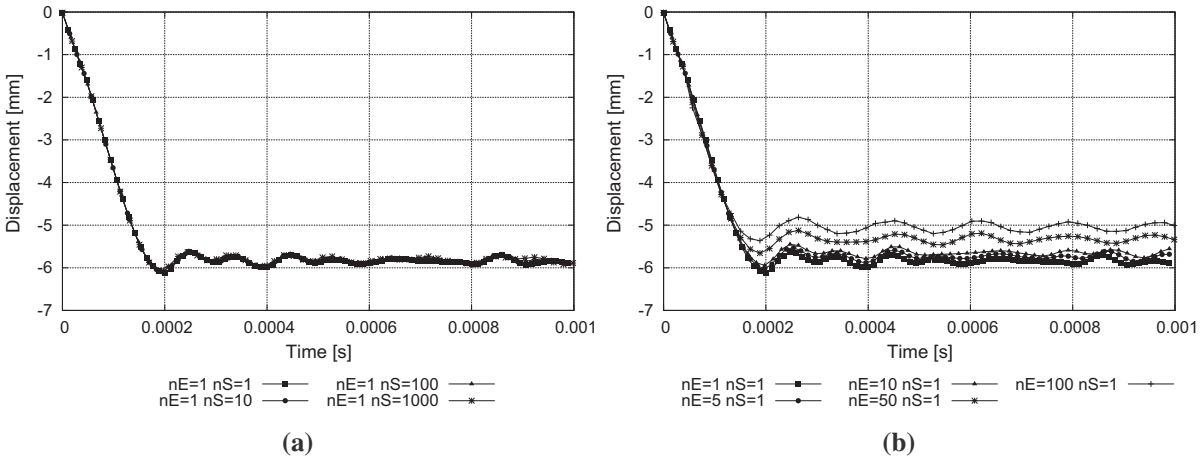

Fig. 12. Explosively loaded rectangular panel. Center point deflection. (a) Dependence on nS, (b) Dependence on nE.

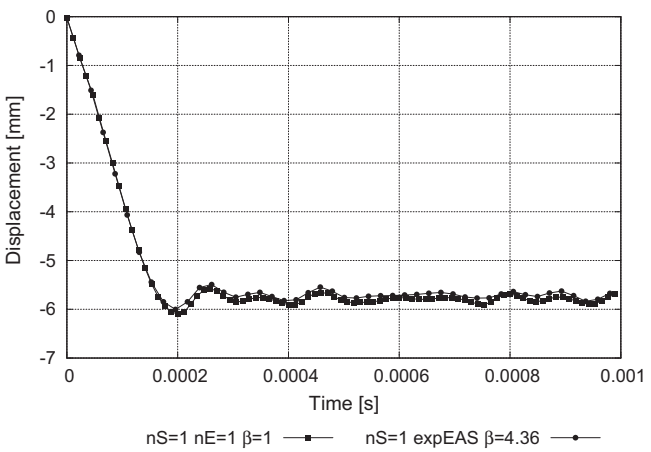

Fig. 13. Explosively loaded rectangular panel. Center point deflection for $nS = 1, nE = 1, \beta = 1$ vs. corresponding curve for $nS = 1, nE = 1, \beta = 4.36$ and *expEAS*.

hourglass stabilization updating every $nS = 10,000$ steps are shown in Fig. 14(a) and (b), respectively. Catastrophic hourglass modes develop very soon in the first analysis, while they are completely absent in the second one. The effect of updating the hourglass term at non-consecutive time steps is also shown in Fig. 15 where no significant differences are seen in the plate center point deflection, independent of the updating frequency. In contrast, the non-stabilized analysis quickly diverges. In conclusion, these results confirm that hourglass control is necessary in explicit dynamics simulations with reduced

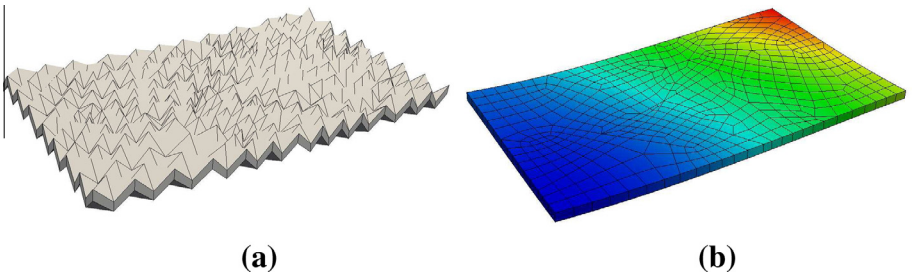

Fig. 14. Explosively loaded rectangular panel. (a) No hourglass stabilization, (b) Hourglass stabilization with $nS = 10000$.

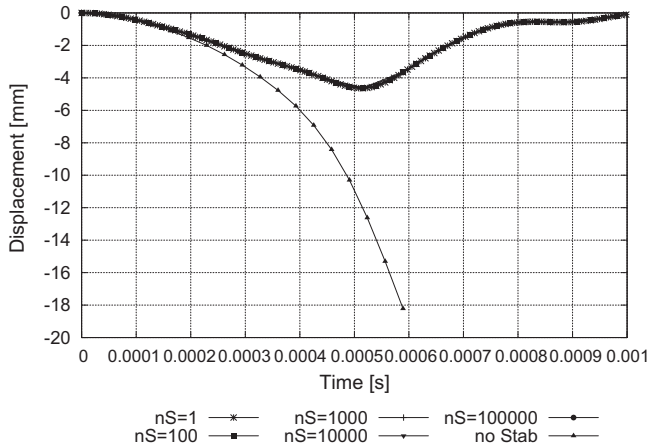

Fig. 15. Explosively loaded rectangular panel. Center point deflection for varying frequency of hourglass stabilization updating.

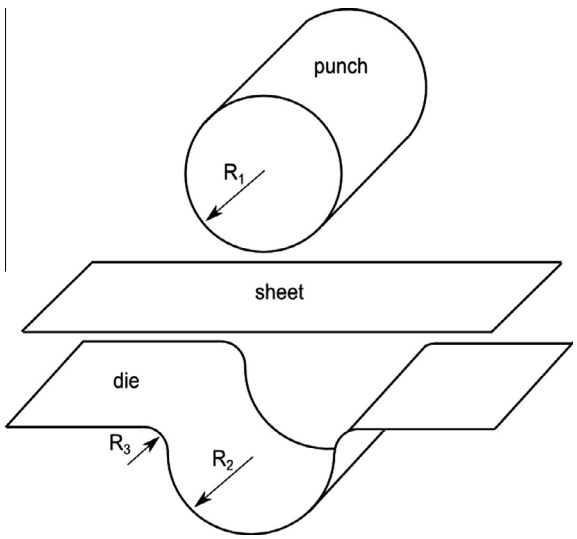

Fig. 16. Tool geometry and set up.

integration solid-shell elements. In the considered cases, the updating frequency has almost no effects on the quality of the results. Numerical tests conducted on initially deformed meshes have confirmed this result (see Fig. 14). The situation might however be different in large strain problems, with significant element distortion occurring as a consequence of the structural deformation. In this case the hourglass stabilization might require to be updated with a higher frequency. Since the maximum computational saving has been shown to be limited to about 12.5% of the original amount, updating with $nS = 100$ is therefore advisable.

4.3. Forming of a rectangular metal strip

The proposed solid-shell finite element has been implemented into the commercial code ABAQUS/Explicit by means of the subroutine VUEL. However, the code does not allow for the full implementation of the selective mass scaling strategy. Therefore, selective mass scaling is not considered in these examples. The benchmark test B of the [27] conference is investigated. Here the bending of an unconstrained metal sheet is considered. Fig. 16 shows the tool set composed of a cylindrical punch of the radius $R_1 = 23.5$ mm and a die characterized by the radii $R_2 = 25.0$ mm and $R_3 = 4.0$ mm. The metal sheet is 120 mm long, 30 mm wide and has a thickness of 1 mm. It is manufactured in aluminum (6111 T4) described by a Young's

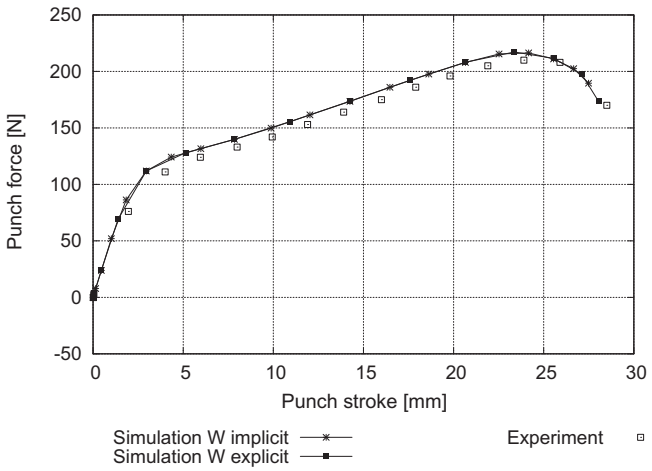

Fig. 17. Punch force vs punch stroke.

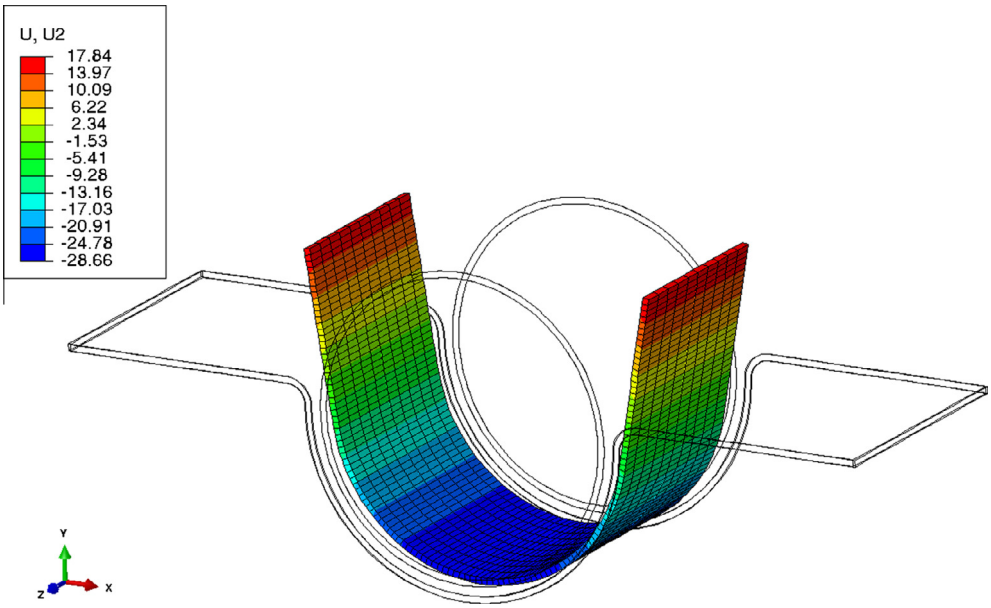

Fig. 18. Deformation at full punch stroke.

modulus of $E = 70500$ N/mm^2, a Poisson's ratio of $v = 0.342$ and a density of $\rho = 2.7 \cdot 10^{-9}$ N s^2/mm^4. The hardening behavior is modeled by a yield stress function of Voce type

$$\sigma_y(\kappa) = 420.1 - 232.7\exp(-8.248\kappa) = \sigma_{y0} + Q(1 - \exp(-\zeta\kappa)) \tag{28}$$

In the latter equation, $\sigma_{y0} = 187.4$ N/mm^2 is the initial yield stress, $Q = 232.7$ N/mm^2 the saturation parameter, $\zeta = 8.248$ the hardening exponent and κ the equivalent plastic strain. The Coloumb friction coefficient between the tools and the sheets reads $\mu_c = 0.1348$.

Due to symmetry, only one quarter of the sheet is modeled. It is discretized by 68×5 elements in the sheet plane and one element over the thickness (including 7 Gauss points). The time step is $\Delta t = 1.305 \cdot 10^{-7}$ s. A tentative application of method (2) has shown that in this more challenging test, where the plate through the thickness response plays a more determinant role, unacceptable modifications of the response are obtained for any value of $nE > 1$. For this reason, only the combination of methods (1) and (3) has been tested in this and in the next example.

Fig. 17 shows the comparison of the punch forces computed by the present finite element formulation without any special provision and using the *expEAS* strategy with $nS = 1000$, with the experimental results of the NUMISHEET'02 contribution BE-01. The agreement between simulation and experiment is highly satisfactory. The deformed system at the final punch stroke of 15 mm is depicted in Fig. 18. The CPU time saving allowed for by the combination of methods (1) and (3) is of about 56%.

4.4. Deep drawing of a square cup

Finally, the deep drawing of a square cup of [26] is also simulated using Abaqus with our VUEL subroutine. An initially quadratic flat aluminum sheet of $150 \times 150 \times 0.81$ mm is fixed between blank holder and die. The geometry of the tool is described in Figs. 19 and 20 . The parameters of the aluminum alloy are given by the Young's modulus $E = 71000$ N/mm^2 and the Poisson's ratio $v = 0.33$. Due to the only mild anisotropy of the aluminum alloy an isotropic material formulation is introduced, characterized by the mean hardening function

$$\sigma_y(\kappa) = \sigma_{y0} + Q(1 - \exp(-\zeta\kappa)) \tag{29}$$

in which $\sigma_{y0} = 132.2253$ N/mm^2 is the initial yield stress, $Q = 459.8124$ N/mm^2 the saturation parameter and $\zeta = 2.6233$ the hardening exponent. In order to model the friction behavior between forming tools and blank the friction coefficient $\mu_c = 0.1348$ is applied. Due to the symmetry of the problem, only a quarter of the sheet is discretized. The mesh includes 32×32 solid-shell elements in the sheet plane. Each solid-shell evaluates the material behavior in five Gauss points over

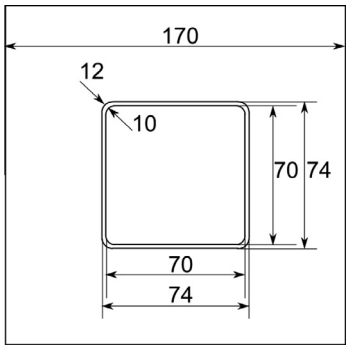

Fig. 19. Geometry of tools.

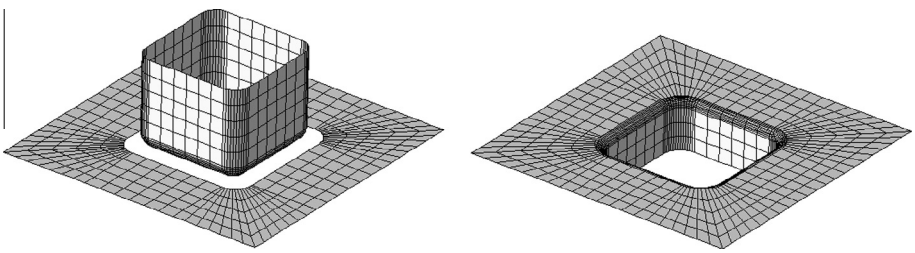

Fig. 20. Punch, blankholder and die mesh.

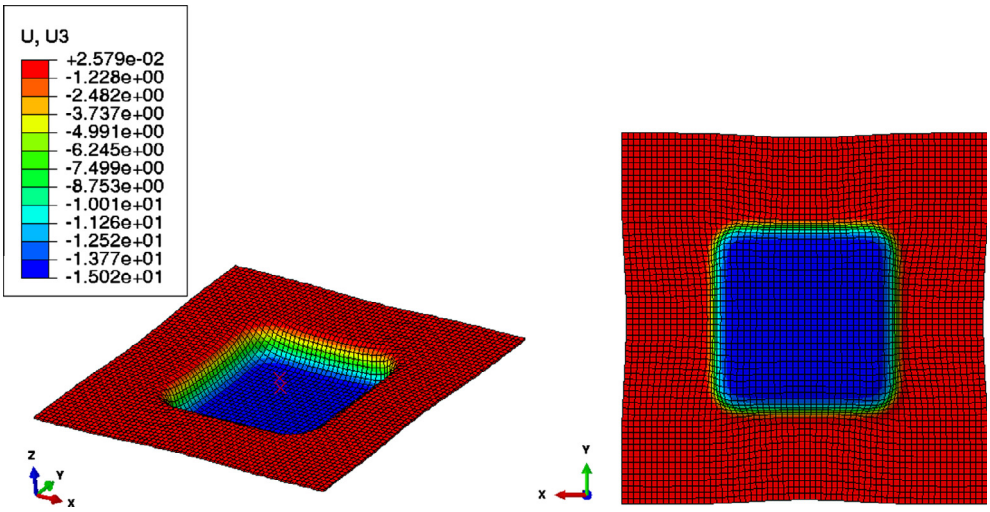

Fig. 21. Final deformation at 15 mm punch travel: perspective and bottom view.

Table 4
Simulation vs. experiment, draw-in punch stroke 15 mm.

	D_x (mm)	D_y (mm)	D_d (mm)
Min. experiment	3.80	3.90	2.30
Max. experiment	6.45	6.49	3.79
Simulation	3.99	4.00	3.11

the thickness direction. The computation has been done using $nS = 10000, nE = 1$ and adopting the *expEAS* strategy. The time step is $\Delta t = 1.168 \cdot 10^{-7}$ s. Also in this case, selective mass scaling could not be used.

The final deformed sheet configuration is shown in Fig. 21. The draw-in measurements of the aluminium sheet at the punch strokes of 15 mm are listed in Table 4. D_x denotes the amount of draw-in along the x-axis, D_y along the y-axis and D_d is the draw-in of the sheet metal corner into the diagonal direction. The minimum and maximum draw-in experimental measurements are reported. In this case, the CPU time reduction obtained by means of the combined use of methods (1) and (3) amounts to about 59%.

5. Conclusions

The results of the paper show that the considered solid-shell element of [32] is well suitable to be applied in explicit analyses. Four techniques have been introduced or applied to reduce the CPU effort. The update of the hourglass stabilization and the internal element degrees-of-freedom is carried out only in each nSth or nEth step, respectively. As an alternative, an explicit estimate of the EAS parameters (*expEAS*), to be used in the next time step, is computed at each time step. In linear problems, or in problems where the through the thickness element behavior does not play a crucial role, the computations show that a reasonable choice for nS and nE is around 100 if the solution should not be significantly altered. In more challenging problems, $nS \leqslant 100$ and $nE = \infty$ should be taken and the *expEAS* strategy should be adopted. The fourth method is the selective mass scaling previously developed in [9]. For this method, applicable to slightly distorted elements, a new technique for the optimal choice of the mass scaling parameter has been proposed and tested. In the discussed examples of a linear-elastic and an elastoplastic cantilever, it has been shown that this technique enables to increase the original time step by a factor almost equal to the element aspect ratio (in-plane dimension over thickness). Overall, we obtain for the non-linear cantilever a reduction of the CPU effort of one order of magnitude with a negligible accuracy loss. Proportionally larger gains would be obtained for smaller thicknesses. The element implementation in Abaqus confirms that a significant gain (more than 50% in the considered tests, where however selective mass scaling could not be implemented) can be achieved with little effort also in commercial codes. Additionally considering the fact that the solid-shell formulation gets by with only a few Gauss points placed along the shell director, it can be concluded that it is in most cases a valuable choice for explicit analysis.

Certainly, the techniques discussed in the present paper have to be investigated further. A larger range of examples has to be examined. A direct comparison with the performance of four-node shells should be made. An interesting aspect for future research is also substructuring which may serve to work with different time steps in different parts of the structure. This is especially advisable for explicit analysis where little communication between the elements is needed.

Acknowledgement

The author Stefanie Reese acknowledges the financial support obtained by the Deutsche Forschungsgemeinschaft (DFG) within the project PAK 343. The authors Mara Pagani and Umberto Perego acknowledge the financial contribution from Tetra Pak Packaging Solutions S.p.a.

References

[1] F. Abed-Meraim, A. Combescure, An improved assumed strain solid-shell element formulation with physical stabilization for geometric non-linear applications and elastic-plastic stability analysis, Int. J. Numer. Methods Engrg. 80 (2009) 1640–1686.
[2] T. Belytschko, J.I. Lin, C.-S. Tsay, Explicit algorithms for the nonlinear dynamics of shells, Comput. Methods Appl. Mech. Engrg. 42 (1984) 225–251.
[3] G. Bergman, M. Oldenburg, A finite element model for thermomechanical analysis of sheet metal forming, Int. J. Numer. Methods Engrg. 59 (2004) 1167–1186.
[4] P. Betsch, E. Stein, An assumed strain approach avoiding artificial thickness straining for a non-linear 4-node shell element, Commun. Numer. Methods Engrg. 11 (1995) 899–909.
[5] C. Bisagni, Dynamic buckling of fiber composite shells under impulsive axial compression, Thin-Walled Struct. 43 (2005) 499–514.
[6] M. Bischoff, E. Ramm, Shear deformable shell elements for large strains and rotations, Int. J. Numer. Methods Engrg. 40 (1997) 4427–4449.
[7] R.P.R. Cardoso, J.W. Yoon, M. Mahardika, S. Choudhry, R.J. Alves de Sousa, R.A. Fontes Valente, Enhanced assumed strain (EAS) and assumed natural strain (ANS) methods for one-point quadrature solid-shell elements, Int. J. Numer. Methods Engrg. 75 (2008) 156–187.
[8] R.P.R. Cardoso, J.M.A. Cesar de Sa, The enhanced assumed strain method for the isogeometric analysis of nearly incompressible deformation of solids, Int. J. Numer. Methods Engrg. 92 (2012) 56–78.
[9] G. Cocchetti, M. Pagani, U. Perego, Selective mass scaling and critical time-step estimate for explicit dynamics analyses with solid-shell elements, Comput. Struct. 127 (2013) 39–52.
[10] R. Eberlein, P. Wriggers, Finite element concepts for finite elastoplastic strains and isotropic stress response in shells: theoretical and computational analysis, Comput. Methods Appl. Mech. Engrg. 171 (1999) 243–279.
[11] D.P. Flanagan, T. Belytschko, Eigenvalues and stable time steps for the uniform strain hexahedron and quadrilateral, J. Appl. Mech. 51 (1) (1984) 35–40.
[12] M. Harnau, K. Schweizerhof, Artificial kinematics and simple stabilization of solid-shell elements occurring in highly constrained situations and applications in composite sheet forming simulation, Finite Elem. Anal. Des. 42 (2006) 1097–1111.
[13] F.J. Harewood, P.E. McHugh, Comparison of the implicit and explicit finite element methods using crystal plasticity, Comput. Mater. Sci. 39 (2007) 481–494.
[14] J. Hetherington, H. Askes, Penalty methods for time domain computational dynamics based on positive and negative inertia, Comput. Struct. 87 (2009) 1474–1482.
[15] T.J.R. Hughes, The Finite Element Method, Prentice-Hall, Englewood Cliffs, N.J, 1987.
[16] K.D. Kim, G.Z. Liu, S.C. Han, A resultant 8-node solid-shell element for geometrically nonlinear analysis, Comput. Mech. 35 (2005) 315–331.
[17] S. Klinkel, F. Gruttmann, W. Wagner, A continuum based three-dimensional shell element for laminated structures, Comput. Struct. 71 (1999) 43–62.
[18] S. Klinkel, F. Gruttmann, W. Wagner, A robust non-linear solid shell element based on a mixed variational formulation, Comput. Methods Appl. Mech. Engrg. 195 (2006) 179–201.
[19] P. Lall, S. Gupte, P. Choudhary, J. Suhling, Solder joint reliability in electronics under shock and vibration using explicit finite-element submodeling, IEEE Trans. Electron. Packag. Manuf. 30 (2007) 74–83.
[20] L.M. Li, Y.H. Peng, D.Y. Li, A stabilized underintegrated enhanced assumed strain solid-shell element for geometrically nonlinear plate/shell analysis, Finite Elem. Anal. Des. 47 (2011) 511–518.
[21] L.M. Li, D.Y. Li, Y.H. Peng, An explicit formulation of solid-shell element and its application in sheet metal forming processes, Adv. Sci. Lett. 4 (2011) 1761–1766.
[22] S. Ma, P. Liu, Modeling of the perfectly matched layer absorbing boundaries and intrinsic attenuation in explicit finite-element methods, Bull. Seismol. Soc. Am. 96 (2006) 1779–1794.
[23] S. Mattern, K. Schweizerhof, Highly efficient solid-shell finite elements for dynamic applications – an implementation concept using symbolic programming, Final report for the DFG proposal SCHW 307/ 20-1, Karlsruhe Institute of Technology, 2011.
[24] S. Mattern, C. Schmied, K. Schweizerhof, Highly efficient solid-shell finite elements for explicit dynamic analysis using symbolic, in: EURODYN 2011, Karlsruhe Institute of Technology, 2012, pp. 1–27.
[25] C. Miehe, N. Apel, Anisotropic elastic-plastic analysis of shells at large strains. A comparison of multiplicative and additive approaches to enhanced finite element design and constitutive modelling, Int. J. Numer. Methods Engrg. 61 (2004) 2067–2113.
[26] A. Machinouchi, E. Nakamachi, E. Onate, R.H. Wagoner (Eds.), Proceedings of the 2nd International Conference and Workshop on Numerical Simulation of 3D Sheet Forming Processes-Verification of Simulation with Experiment, NUMISHEET'93, 1993, Isehara, Japan.
[27] D.-Y. Yang, S.I. Oh, H. Huh, Y.H. Kim (Eds.), Proceedings of the 5th International Conference and Workshop on Numerical Simulation of 3D Sheet Forming Processes-Verification of Simulation with Experiment, NUMISHEET'02, 2002, Jeju Island, Korea.
[28] L. Olovsson, M. Unosson, K. Simonsson, Selective mass scaling for thin walled structures modeled with tri-linear solid elements, Comput. Mech. 34 (2004) 134–136.
[29] L. Olovsson, K. Simonsson, M. Unosson, Selective mass scaling for explicit finite element analyses, Int. J. Numer. Methods Engrg. 63 (2005) 1436–1445.
[30] M. Pagani, S. Reese, U. Perego, Explicit simulation of forming processes using a novel solid-shell concept based on reduced integration, Key Engrg. Mater. (2012) 425–430.
[31] S. Reese, A large deformation solid-shell concept based on reduced integration with hourglass stabilization, Int. J. Numer. Methods Engrg. 69 (2007) 1671–1716.
[32] M. Schwarze, S. Reese, A reduced integration solid-shell finite element based on the EAS and the ANS concept – Large deformation problems, Int. J. Numer. Methods Engrg. 85 (2011) 289–329.
[33] J.C. Simo, F. Armero, Geometrically non-linear enhanced strain mixed methods and the method of incompatible modes, Int. J. Numer. Methods Engrg. 33 (1992) 1413–1449.
[34] X.G. Tan, L. Vu-Quoc, Efficient and accurate multilayer solid-shell element: non-linear materials at finite strain, Int. J. Numer. Methods Engrg. 63 (2005) 2124–2170.
[35] M. Vrh, M. Halilovič, B. Štok, Improved explicit integration in plasticity, Int. J. Numer. Methods Engrg. 81 (2010) 910–938.
[36] J.T. Wang, T. Chen, D.W. Sleight, A. Tessler, Simulating Nonlinear Deformations of Solar Sail Membranes using Explicit Time Integration, AIAA, 2004. pp. 1–15.
[37] H.J. Xu, Y.Q. Liu, W. Zhong, Three-dimensional finite element simulation of medium thick plate metal forming and springback, Finite Elem. Anal. Des. 51 (2012) 49–58.